Journal of Nuclear Materials 533 (2020) 152094

Contents lists available at ScienceDirect

Journal of Nuclear Materials

journal homepage: www.elsevier.com/locate/jnucmat

Microstructure evolution in MA956 neutron irradiated in ATR at 328 °C to 4.36 dpa

Zhexian Zhang [a,*], Tarik A. Saleh [b], Stuart A. Maloy [a,b], Osman Anderoglu [a]

[a] Nuclear Engineering Department, University of New Mexico, Albuquerque, NM, 87131, USA
[b] Materials Science and Technology Division, Los Alamos National Laboratory, Los Alamos, NM, 87545, USA

GRAPHICAL ABSTRACT

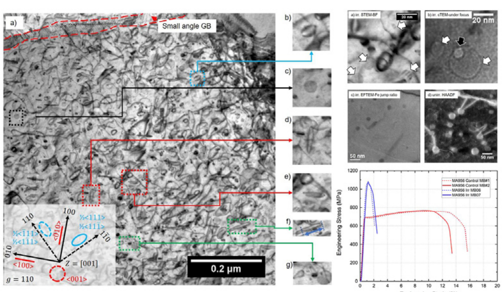

ARTICLE INFO

Article history:
Received 5 December 2019
Received in revised form
3 March 2020
Accepted 4 March 2020
Available online 10 March 2020

ABSTRACT

MA956 is an iron-chromium-aluminum (FeCrAl) based oxide dispersion strengthened (ODS) alloy produced by mechanical alloying. The alloy was irradiated in the Advanced Test Reactor (ATR) at 328 °C up to 4.36 dpa with both thermal and fast neutrons. The microstructures before and after irradiation were investigated by various TEM techniques. The size and number density of dislocation loops, voids, and oxides were analyzed. The results showed that both 1/2<111> and <100> loops were generated in irradiated materials. The number density of dislocation loops reached up to $7.17 \times 10^{21}/m^3$. Cavities/voids were formed during irradiation. Argon bubbles were observed in unirradiated materials attached to the surface of oxide particles. The swelling rate was estimated to be 0.08% without subtracting pre-existed Ar bubbles. The oxide particles could maintain crystal structure during irradiation. The oxides had small decrease in size but half reduction in number density after irradiation. Calculation estimated that <100> loops and dislocation lines contributed most to hardening. Alpha prime precipitates were suggested to be formed by comparing to the calculated hardening. Dislocation lines are demonstrated not forming tangles in irradiated specimens.

© 2020 Elsevier B.V. All rights reserved.

1. Introduction

Current designs for nuclear reactors like GenIV and fusion reactors require high performance of structure materials in extremely hostile environment, including high temperature, intense neutron fluxes and aggressive coolant [1,2]. Meanwhile accident tolerant fuel (ATF) cladding materials for light water reactors (LWR) need to

* Corresponding author. Nuclear Engineering Department, University of New Mexico, Albuquerque, NM, 87131, USA.
E-mail addresses: zx-zhang@iae.kyoto-u.ac.jp (Z. Zhang), tsaleh@lanl.gov (T.A. Saleh), maloy@lanl.gov (S.A. Maloy), oanderoglu@unm.edu (O. Anderoglu).

https://doi.org/10.1016/j.jnucmat.2020.152094
0022-3115/© 2020 Elsevier B.V. All rights reserved.

have high oxidation resistance and good mechanical property at high temperature in beyond-design scenarios [3,4]. To this end, alternative candidates to traditional Zr-based alloys has been proposed, including modified/coating Zr-alloys, full ferritic Fe−Cr system steels, C-bearing ferritic/martensite (F/M) steels, refractory alloys, ceramics like SiC, and high entropy (HEA) concept alloys [5–7]. Among these candidates, the full ferritic steels are the most promising for in-core applications [4,7–9]. On one hand, the Fe−Cr−Al system could form a protective Al_2O_3 layer in high temperature steam that meet the corrosion resistance demand for ATF materials. It has been proved that a commercial FeCrAl based steel APMT satisfies the X100 reduction in oxidation rate constant compared to Zr-alloys [10]. On the other hand, with oxide dispersion strengthening (ODS), the steels will enhance the creep and fatigue resistance over a wide range of temperature by pinning dislocations and grain boundaries [11]. At the same time, the dispersoids will improve the swelling tolerance by offering the sink site for vacancy and interstitial recombination under irradiation [11,12]. The uniformly distributed nanometer size oxide particles can also prevents embrittlement by trapping transmutant helium (He) into fine and less harmful bubbles [13].As a result, the FeCrAl ODS steels have required excellent corrosion resistance, irradiation resistance and high temperature mechanical properties.

The operation temperature window for ODS ferritic steels is 300–700 °C [14]. Issues limiting the application of FeCrAl ODS steels under irradiation include 1) the irradiation embrittlement due to formation of dislocation loops and cavities, 2) phase stability and radiation induced segregation (RIS), and 3) the oxides stability, particularly the amorphization and dissolution. These issues are related to the chemical optimization and operation environment designs. For example, Cr could enhance the corrosion resistance and impede dislocation loops formation during irradiation, but high Cr content will cause aging embrittlement by α' precipitation. Al could benefit to the oxidation resistance [15] and shift the miscibility gap of Fe−Cr to higher Cr direction [16] but trade off the tensile strength by coarsening the oxide particles [15]. The Ti-bearing (Al-free) ferritic ODS steels have lower swelling rate than Zr-bearing steels because of coarsen oxide particles owing to Al and Zr [17], however, Y−Ti−O oxides seems not as stable as Y−Zr−O or Y−Al−O oxides under irradiation environment [18]. Therefore, designs for ODS steels need considering the balance on the Cr and Al content, and proper bearing element like Ti, Zr, Hf and so on.

MA956 is an old commercial ferritic ODS steel and discontinued from market due to lack of industry demand [19]. The nominal composition of MA956 is Fe−20Cr-4.8Al-0.4Y_2O_3-0.4Ti. Detail composition was listed in Table 1. MA956 was considered only useful as a surrogate for an ATF FeCrAl ODS variant because optimized GenII ATF ODS FeCrAl have much improved ductility ensuring easier tube fabrication [20]. Mechanical properties of MA956 can be found in its commercial database [21]. Researches on unirradiated MA956 ranges from recrystallization, texture, DBTT and corrosion/oxidation [22–27]. Although these alloys are all called MA956, yet have four market shapes, e.g. sheet/plate and tube/bar, with different post-extrusion processing (rolling and annealing), that the microstructures and mechanical properties will be different to each other. The MA956 used in this study is in plate shape. It was produced from mechanical alloying (MA) with pre-alloyed powder (Fe−Cr−Al−Ti), yttria (Y_2O_3) and elementary powder (Fe, Cr) in Ar shielding atmosphere [28–30]. After MA, the powders were consolidated by hot-extrusion. The consolidated billet was hot-rolled at 1050 °C to a thickness of 9.7 mm. The direction of hot-rolling was perpendicular to the direction of hot-extrusion. This cross-rolling yielded pancake-shape grains in the final plate.

Previous ion-irradiation in MA956 investigations were focusing on the oxide evolution and swelling behavior. The oxide particles of self-irradiated MA956 at 450 °C to 60–180 peak dpa tend to increase in size but reduce in number density [31]. This phenomenon might be explained as Ostwald ripening where dissolution of small nanoparticles (NPs) will redeposit onto or be absorbed by larger NPs [32]. The self-irradiation up to 2.4–60 peak dpa at 450 °C however, have constant oxide diameter but reduced number density [33]. Dual beam (Fe + He) simultaneous irradiation showed a helium shell around oxide core in MA956 at 425 °C [34]. Heavy Neion implantation experiments revealed MA956 has smaller void growth at grain boundaries than F/M Grade 92 steel [35]. As for neutron irradiation, Gelles investigated various steels irradiated in the Fast Flux Test Facility (FFTF) at 420 °C to 200dpa [36]. The results showed the swelling of MA956 as well as MA957 measured by density change is only about 1%, indicating the commercial ferritic ODS steels are extremely resistant to radiation induced void swelling. Krumwiede et al. have reported the tensile test behavior of MA956 and other ODS steels after neutron irradiation [37]. The MA956 showed severe irradiation hardening and ductility reduction compared to Al-free 14YWT ODS steel.

In this study, we investigated the microstructure evolution of neutron irradiated MA956. The irradiation temperature was 328 °C which is in the typical light water reactor (LWR) operating temperature range. Three issues were addressed for the microstructure characterization. The first is statistical analysis of dislocation lines, loops and voids which contribute to the irradiation hardening and embrittlement. Particularly, the nature of dislocation loops, glissile ½<111> or sessile <100> Burgers vectors were identified. The second is α' precipitates which is essential in thermal aging but could be affected by irradiation. Even though we found no obvious α' precipitates via current TEM techniques, they should be theoretically existed in this high Cr steel at the experiment temperature range. It is speculated that the resolution of TEM could not meet the minimum contrast requirement to recognize these fine precipitates. The third is oxide stability, including crystalline/amorphous and growth/dissolution behavior. These issues were characterized by TEM Moiré fringes and size/number density respectively. We also attached the tensile results of MA956 before and after irradiation. Finally, the irradiation hardening was calculated with Orowan equations and compared to the tensile yielding stress. The results will exhibit the microstructure morphology under irradiation and contribute to the database of neutron irradiated ODS steels.

2. Experimental

The irradiation in this paper is part of the large multipurpose program led by University of California Santa Barbara as part of the Advanced Test Reactor (ATR) Nuclear Science Users Facility (NSUF) Program [38]. As-received MA956 plates were obtained from Special Metals Corporation. The composition of the main elements is

Table 1
Chemical composition of MA956 [21].

Fe	Cr	Al	Y_2O_3	Ti	Cu	Ni	Co	Mn	C	S
Bal	18.5–21.5	3.75–5.75	0.3–0.7	0.2–0.6	<0.15	<0.50	<0.3	<0.3	<0.1	<0.02

listed in Table 1. Fabrication of these plates has been introduced in Section 1. Neutron irradiation was carried out in ATR with pressurized light water coolant at Idaho National laboratory (INL) [39]. The neutron spectrum covered a wide range from 1×10^{-9} MeV−10 MeV. At the reactor power of 110MWth, the thermal neutron flux was about 2×10^{14} n/cm^2-s while the fast neutron (E > 1 Mev) flux was around 2.3×10^{14} n/cm^2-s [40]. The samples were located at "A" capsule positions in ATR core and irradiated to accumulatively 4.36 dpa at 328 ± 10 °C. The operating powers were between 108 and 116MWth. The total neutron fluences at each energy were given in Fig. 1.

TEM specimens were produced using an FEI Quanta and a Helios 600 DualBeam focused ion beam (FIB) micromachining. Both sides of the specimen were milled with 1 kV Ga^+ as a final step to minimize the damage from FIB. The microstructures were observed in FEI Tecnai F30 Super-Twin TEM. The electron beam source was provided by the field emission electron gun with the accelerating voltage at 300 kV. Both conventional TEM (cTEM) and Scanning TEM (STEM) mode were used to image the irradiation induced defects. In cTEM mode, the incident beam was parallel. The specimen was tilted to two beam kinematic condition with deviation parameter slightly positive and the dislocations were imaged closed to [001] zone axis with g equals (110). In STEM mode, a convergent beam was scanned on the specimen with the smallest convergent angle by inserting the smallest condenser aperture to avoid overlapping of systematic patterns which will generate phase contrast instead of diffraction contrast. The invisible criterion under STEM mode was demonstrated similar to that in cTEM [41]. During the practical operation, the specimen was first tilted to two beam condition in cTEM mode and then changed to STEM mode to make sure they have exactly the same diffraction condition. The imaging of dislocations in STEM mode could be on zone axis as well [42,43]. The details of the dislocation contrast imaging in STEM mode will be discussed and published elsewhere.

The thickness of TEM specimen (t) was obtained from a relative thickness map using EFTEM utilizing equation (1)by considering the Poisson statistics of inelastic scattering. The I_0 stands for the integral of zero-loss peak and I_t for the total integral of the EEL spectrum. The values of I_0 and It corresponded to the intensity at each pixel in zero-loss image and unfiltered image respectively. The mean free path (λ) was calculated with the collection (semi-) angle β set to 100 mrad because no objective aperture was inserted, that the scattering cross section will be independent of β above this value. The mean atomic number was 26 as it is Fe based alloy. The calculation method could be found in Ref. [44].

$$t / \lambda = -ln(I_t / I_0) \tag{1}$$

Line intercept method was used to measure dislocation density. In equation (2), ρ means the dislocation line density, N is the total intersections, l is the total line length, t is the thickness of specimen. The coefficient $\alpha = 2$ by assuming the dislocations are spatially random oriented [45].

$$\rho = \alpha N / lt \tag{2}$$

Dislocation loops were measured under STEM two-beam like diffraction condition. The axis was chosen to be [001] and g vector parallel to (110). The diameter of dislocation loop is determined by the long axis of the projected eclipse.

Cavities were examined by out-of-focus method. The cavities will be bright at defocus condition in cTEM due to phase contrast. The voids were imaged with defocused beam where no diffraction pattern was strongly excited.

The α' precipitation was examined by EFTEM jump ratio technique using one pre-edge and one post-edge of Cr to pick out the Cr concentrated or depleted part.

Oxides were examined via various TEM techniques. The oxides in unirradiated materials were imaged in STEM-HAADF mode where Z-contrast was dominate. The advantage of this mode is little moiré fringes shown compared to bright field that affect the precision of oxide size measurement. The diffraction contrast still remains owing to the relatively large collection angle. In this case, both the dislocations and oxides have bright contrast. As the beam intensity is much higher in STEM mode, a thicker area ($t > 140$ nm) can be investigated to increase the accuracy of measurement. For the irradiated materials, we performed EFTEM to avoid the overlapping of contrast of high dense dislocation lines and oxides in diffraction-based method. The images were taken in thin area($t < 90$ nm) to ensure enough electrons collected.

Tensile tests were performed on 30 kN capacity Instron 5567 screw driven load frame in the Wing 9 hot cells at the Chemistry and Metallurgy Research Facility (CMR) at LANL. Tests were performed at constant cross head velocity of 0.15 mm/min corresponding to an initial strain rate of 5×10^{-4}/s. The tensile samples are typical S1/SSJ2 type, with 0.5 mm thickness, 5 mm gauge length and 1.2 mm width. The tensile experiments were performed at room temperature.

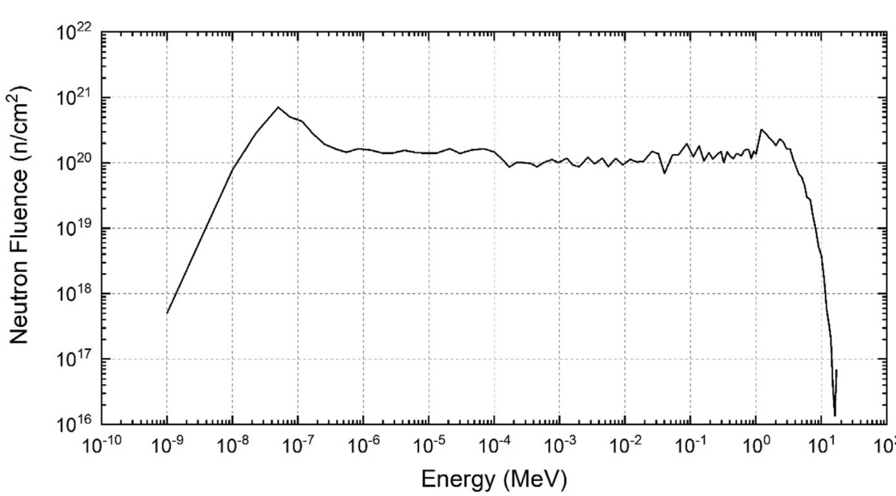

Fig. 1. Summation of neutron fluence vs energy at experiment reactor powers.

3. Results

3.1. Overview of microstructures in unirradiated MA956

The overview of the microstructures of an unirradiated reference MA956 is shown in Fig. 2a. The grains are elongated in one direction because of mechanical processing. While the average width of the grains is about 0.5 μm, the length is more than 1 μm which leads to a grain aspect ratio (GAR) larger than two. To identify if there is any preferred grain orientation, the selected area aperture was inserted to the center of Fig. 2a with grains included as many as possible. The coincided diffraction pattern attached on the left top corner in Fig. 2a indicated these grains sharing a preferred crystal orientation. Coarse estimation showed the viewed plane (cross-section of the rolled plate) is close to (110) <110><001> corresponding to a strong <110> α-fiber to the elongated direction in cross-rolled ferritic steels [46]. The sub-grain boundaries could be seen across the elongated grains. The low angle sub-grain boundaries could be viewed as dislocation walls or networks for titled or twisted boundaries respectively. Further investigation showed the dislocations inside the grains are at a very high density because of working hardening. Fig. 2b shows an enlarged region of interest (ROI) where Ar bubbles are attached to one side of the oxides. These bubbles were formed during MA processing with Ar as protection gas [47]. Existence of Ar bubbles indicates the reference materials did not reach to their full mass density.

3.2. Irradiation induced dislocation loops and voids in MA956

3.2.1. Dislocation loops

The irradiated specimen was observed under STEM bright field (BF) mode. The orientation was tilted close to [001] zone axis. Images were taken under two beam condition with reflecting vector g=(110). In BCC materials, the burgers vectors of irradiation induced dislocation loops are 1/2<111> and <100> types. Note that there are totally four types of 1/2<111> and three types of <100> in crystallography. The irradiation induced dislocation loops were pre-assumed to be pure edge type that the habit plane could be read out directly from their Burgers vectors. Assuming the dislocation loops are perfect round circles, then the projected loop images could be calculated by equations (3) and (4).

$$\vec{l} = \vec{Z} \times \vec{b} \tag{3}$$

$$b/_a = |\cos\theta| \tag{4}$$

Where $\vec{l}$ is the orientation of projected loop (long axis), $\vec{Z}$ is the observation zone axis, $\vec{b}$ is the Burgers vector of dislocation loop, b and a stand for the short axis and long axis of the projected eclipse respectively, θ is the angle between zone axis and burgers vector, which equals to the complementary angle between project plane and habit plane.

Yao et al. [48] has summarized the relationship between projected images of dislocation loops and their Burgers vectors. Here we recalculated the relationship under the [001] zone and re-indexed in the right-handed coordinate system. Fig. 3 shows the bright field images in STEM mode. In Fig. 3a, dislocation loops could be seen along a typical orientation. When viewed from [001] zone axis, all the 1/2<111>type dislocation loops will have the ratio b/a = 0.577. At the same time, 1/2<111> and 1/2<11−1> will be projected along [1−10] direction, as shown in Fig. 3b, and the 1/2<−111> and 1/2<1−11> loops will be projected along [110] direction. The oxides are perfect round solid circles as shown in Fig. 3c. The <100> and <010> loops will have b/a = 0 and should exhibit as a line or slim eclipse owing to sample tilting. They will extend to [010] and [100] respectively, as shown in Fig. 3d and e. The <001> loops whose habit plane is perpendicular to the zone axis, will be a round unfilled circle.

When g= (110), the 1/2<−111>, 1/2<1−11> and <001> loops will be invisible. However, there are some other loops found in the specimen. Fig. 3f shows an example of a slim loop that extends along the [1−10] direction which does not obey any of the aforementioned rules. The reason could be owing to the surface effect that the loop changed its orientation, or the inside contrast instead of outside contrast that made it looks slim. We do not expect it to be a <110> type loop because they should not be induced by irradiation in BCC materials at high temperature.

The size distribution of dislocation loops is summarized in Fig. 4. A total of 176 loops were measured with a Java programmed tool ImageJ [49]. The curves were log-normal fitted instead of a Gaussian distribution. Most of the loops were distributed within 5−25 nm, while the largest loop size was over 60 nm. The distribution of the measured loops ignored invisible loops in TEM images. If considering the extinction criterion, the actual number density of loops corresponds to 7.17 × 10^{21}/m^3.

3.2.2. Voids and swelling

Swelling occurs when vacancies start to migrate above the Stage

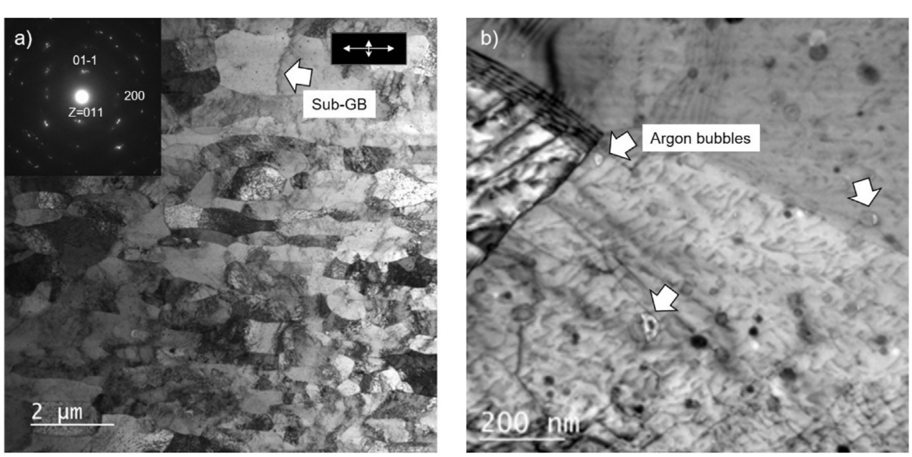

Fig. 2. The TEM images of reference MA956, a) the overview of grain morphology and b) the Ar bubbles attached to one side of oxide particles.

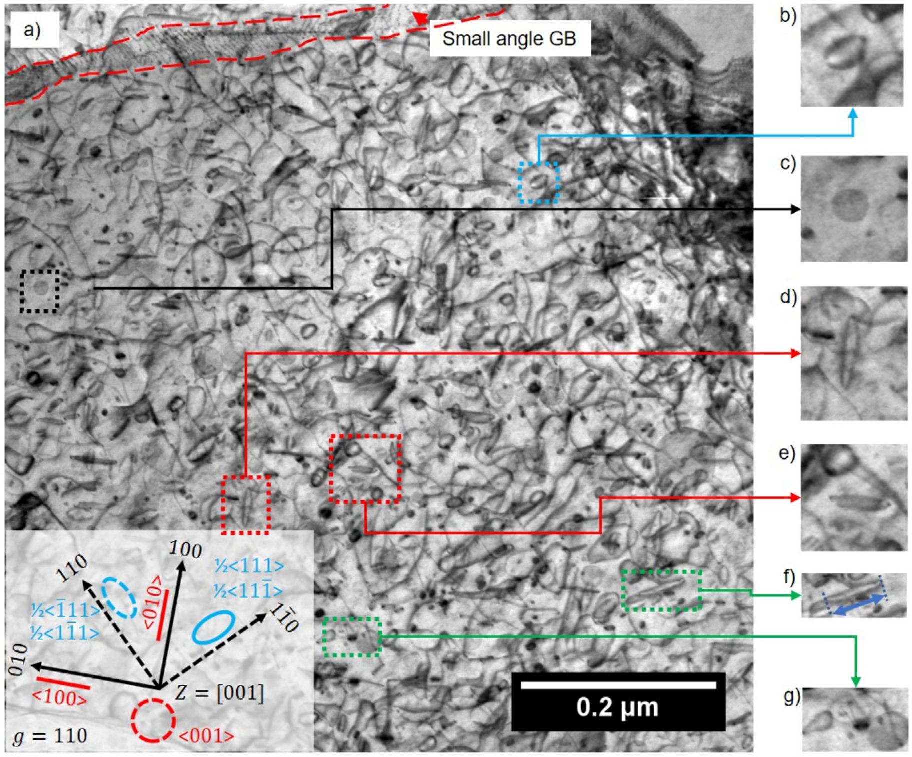

Fig. 3. a) the STEM bight field (BF) images of irradiated MA956, b) 1/2<111> or 1/2<11−1> dislocation loop, c) oxide particle d) <010> loop, e) <100> loop, f) a loop with unknown Burgers vector, and g) a loop showed as black dots.

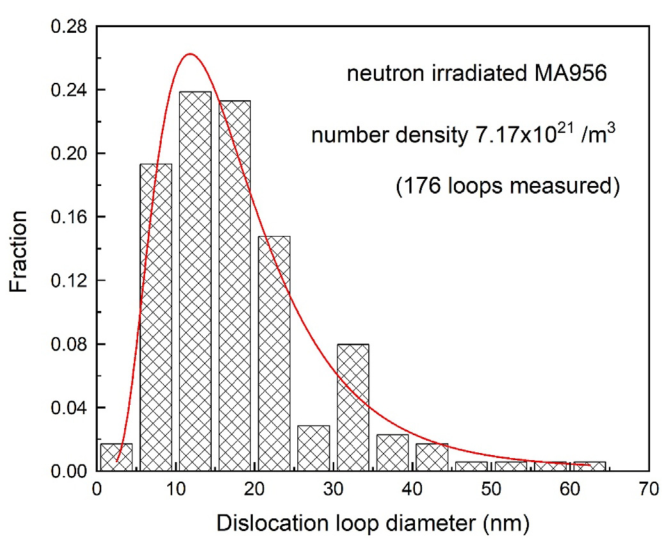

Fig. 4. Size distribution of dislocation loops in irradiated MA956.

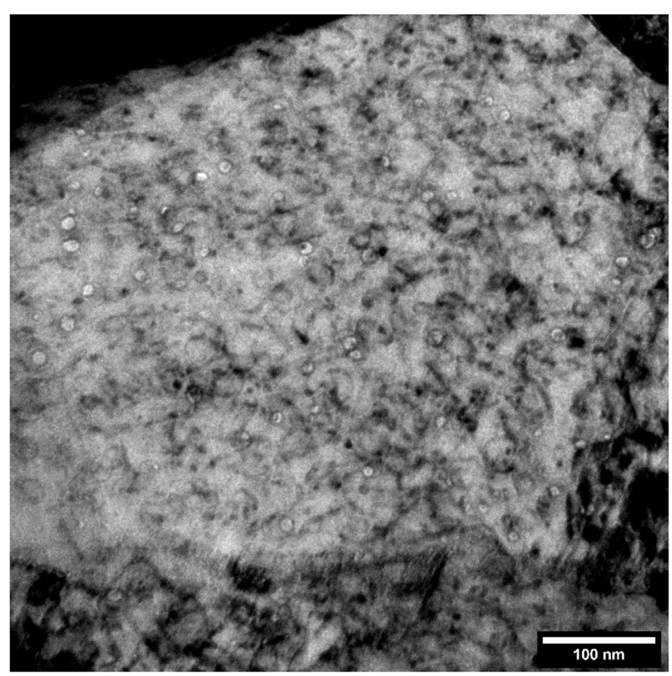

Fig. 5. Under-focused TEM image shows the voids in MA956 after neutron irradiation.

III temperature range. In neutron irradiation, transmutant helium may combine with vacancies and form into stable helium-vacancy complexes. Typically, cavities without gas atoms are named voids, while the cavities containing inert gas are called bubbles. However, to distinguish from Argon bubbles which already existed in the reference materials, the cavities induced by neutron irradiation are called voids here, regardless of amount of helium in them.

Fig. 5 shows the void morphology in MA956 after neutron irradiation. Although some of those are Ar bubbles attached to the oxide particles as previously mentioned in Fig. 2b, most of the voids are free and randomly distributed inside the grains. The average size of the voids is 8.7 ± 2.9 nm, and the number density is $1.80 \times 10^{21}/m^3$. There is no preference of voids being attracted to grain boundaries or any void denuded zone. As it is difficult to distinguish the Ar bubbles and voids under current TEM method, the estimated size and number density of voids and further swelling ratio are with Ar bubbles included. Even the density of Ar bubbles cannot compare to the voids, the swelling could be overestimated by current method.

The way to calculate swelling via TEM images uses the following equation [50]:

$$\%\Delta V/_{V} = 100\left[\Delta V \Big/ \left(V_f - \Delta V\right)\right] \tag{5}$$

$$\Delta V = \sum_i \frac{1}{6}\pi d_i^3 \tag{6}$$

$$V_f = At \tag{7}$$

Where ΔV is the change in volume, V is the original volume of the material, V_f is the final volume of the material, d_i is the diameter of the ith void, A is the area of the TEM image, t is the sample thickness.

The swelling rate calculated by equation (5) is approximately 0.08%. The volume of Ar bubbles is estimated to be 0.007%. As there are few reports on neutron irradiated MA956, we cannot precisely evaluate the swelling per dpa at this temperature directly. The swelling in neutron irradiated Fe–Cr binary alloys has been summarized by Garner et al. [51] and 0.2%/dpa post transient swelling rate is reported after incubation. The concentration of Cr however, may suppress the swelling at high temperatures. When irradiated at ~450 °C, 15%Cr showed reduced swelling than 10%Cr, but when irradiated ~400 °C, swelling in 15%Cr was much greater than 10%Cr [51,52]. In Cr^+ irradiated MA957, peak swelling occurred between 420 °C and 450 °C [53]. The results showed MA957 has a higher onset swelling dose than EP450 and HT9. It is likely that the fine oxide dispersion suppressed void formation. In the case of the Fe–Cr–Al ternary system, Field and his coworkers found a small number of cavities in FeCrAl alloys at around 400 °C to 1.8 dpa, which may help demonstrate the effect of Al on swelling [54]. However, Song et al. showed that after helium implantations, Al-free Fe–Cr ODS steel showed less swelling than FeCrAl ODS steel in the temperature range from 300 °C to 700 °C [17]. In the current study, we only observed a small amount of swelling induced by neutron irradiation in MA956. More research needs be done on this type of Al-added Fe–Cr ODS steels in the future to understand the swelling behavior thoroughly.

3.3. Alpha-prime precipitates

Cr is an important element to raise the corrosion resistance in Fe based steels. However, distribution of Cr may be inhomogeneous. The Cr may form into Cr-rich α' precipitates [55–59], form a shell structure around oxides [60,61], and deplete from or concentrate at grain boundaries owing to RIS [43,62–64]. In aging experiments at 475 °C after 2000 h, the FeCrAl-ODS steels with 12%–18% Cr (wt%) showed aging embrittlement due to α' precipitate [60]. Irradiation accelerated formation of α' is well established in both FeCr binary alloys [56] and FeCrAl ternary alloys [57]. Although high Cr content (>30 at%) will lead to spinodal decomposition, the α' in this study's range should experience a nucleation/growth procedure, according to recent study on Fe–Cr phase diagram [65]. The additive Al however, can impede the formation of α' during irradiation [66]. Irradiation mixing may induce concentration variation that enhance the precipitate process. Fig. 6 shows the EFTEM jump ratio images of Fe and Cr in the irradiated materials. The investigation did not indicate any α' in the matrix or core-shell structures around oxides. However, a recent study of Fe-18 at% Cr irradiated in similar neutron environment shows α' precipitates by atom probe

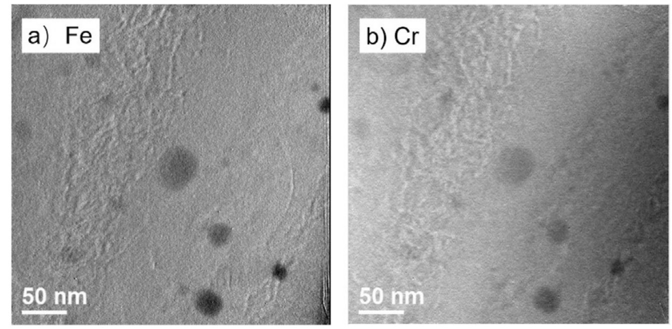

Fig. 6. EFTEM of a) Fe and b) Cr jump ratio images, which showed no obvious α' precipitate in the matrix at this imaging technique.

tomography (APT) method [58]. Another Al-free steel, 14YWT, also showed α' precipitates after irradiations up to 7dpa at 360–370 °C [67]. Briggs et al. performed neutron irradiations to FeCrAl steels similar to MA956 [68]. The Fe-17.5Cr–3Al (wt%) steel was irradiated in High Flux Isotope Reactor (HFIR) at 320 °C to 7dpa. The results by small-angle neutron scattering (SANS) analysis showed the α' precipitates have average size of 2.5 nm with number density of $0.7 \times 10^{24} m^{-3}$. The reason that $\alpha'$was not observed in this paper could be owing to the small size of precipitates that exceeded the TEM technique limitation.

3.4. Oxides

There are various types of particles in Al-bearing ODS materials like MA956. The alumina particles (Al_2O_3) could be around 500 nm while titanium carbonitrides Ti(C,N) are about 100–200 nm [69]. Both of the particles are at very low densities and are not interesting in this study. The Y–Al–O particles however, with an average size of 10 nm and a density of up to $5x10^{21} m^{-3}$ [70], will contribute the most as trapping sites to the interstitials and vacancies induced by irradiation. The Y–Al–O particles could be YAP ($YAlO_3$, perovskite), YAG ($Y_3Al_5O_{12}$, garnet), YAM ($Y_4Al_2O_9$, monoclinic), YAP' (YAO_3, pseudo-perovskite), YAH ($YAlO_3$, hexagonal), and YAT ($Y_3Al_5O_{12}$, tetragonal) [71]. The formation of oxide particles depends on annealing time and temperature [72], but may also be related to other factors such as Ti concentration [73]. Previous literatures showed lattice images of both YAT structure [35] and YAM structure [31] in MA956 using HRTEM. The X-ray diffraction (XRD) spectrum of extracted particles revealed that the oxides contain both YAP and YAG [74]. A study from diffraction pattern of dispersoids retrieved in carbon replica and STEM-EDS composition analysis claimed that most of the particles are YAP while about 10% are probably YAM [70].

Fig. 7 shows the oxide particle images using different TEM techniques. Fig. 7a shows the irradiated specimen using STEM-BF technique under two beam condition. One can see the coexistence of dislocation loops and oxide particles. Most of the oxide particles showed moiré fringes owing to the lattice misfit between particles and matrix. Fig. 7b shows the particles by under-focused cTEM. The specimen was tilted to avoid exciting any diffraction pattern. At this condition, diffraction contrast is suppressed, and voids will show up clearly. The black arrow in Fig. 7b indicates a void attached to the surface of an oxide particle, which can be considered as an evidence that the particles could act as a sink site for vacancy type defects. EFTEM was used to analyze particle size because dislocations will not appear in these images. Fig. 7c applied the jump ratio technique choosing one pre-edge and one post-edge of Fe to pick out the Fe depleted part, where the oxide particles will

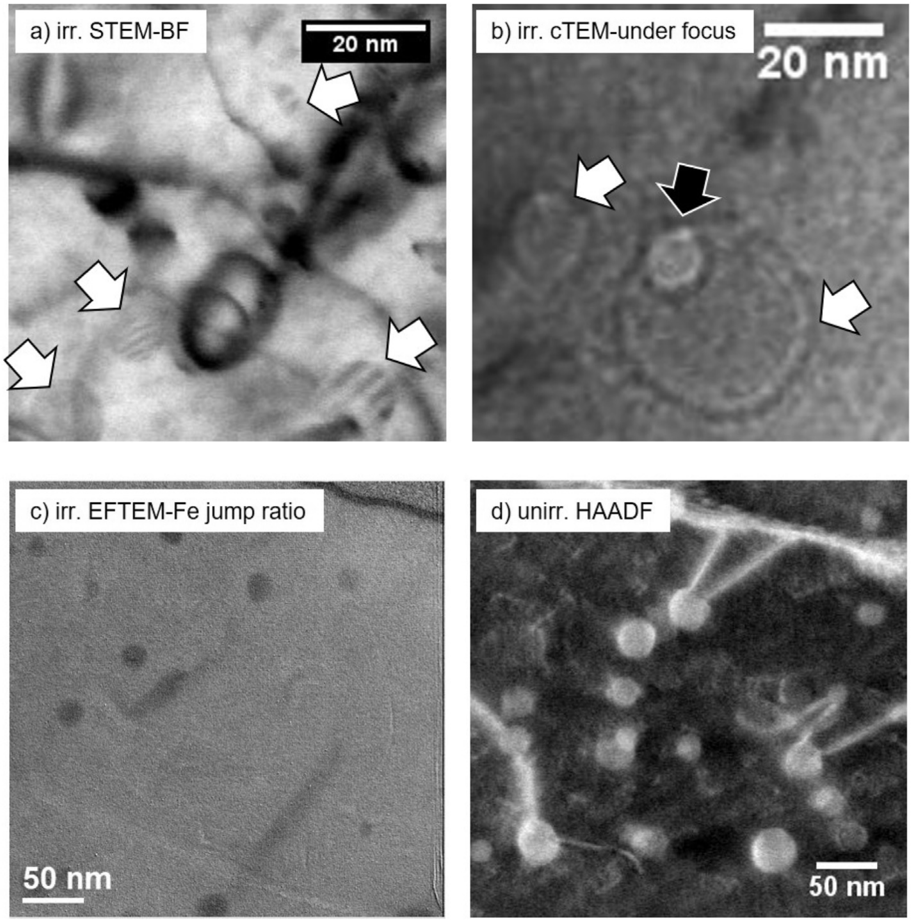

Fig. 7. The TEM images of oxide particles, the white arrows point to oxides and the black to voids, a) coexistence of dislocations and oxides, the moiré fringes indicate oxides remained crystal structure after irradiation, b) void attached on the surface of oxide, c) EFTEM image for oxides analysis after irradiation, where dislocation lines/loops did not show contrast, and d) STEM HAADF image for oxides characterization before irradiation, where dislocations and oxides showed strong bright contrast. (irr = irradiated, unirr = unirradiated).

show dark contrast. Compared with the irradiated specimen, an unirradiated one was imaged by STEM-HAADF, as shown in Fig. 7d. In this condition light elements will appear dark and heavy elements bright, following the Z-contrast rules. However, the dislocations will still appear bright when camera length is not small enough, where certain planes giving strong reflection absorbed by the HAADF detector that diffraction contrast will remain in the dark field image. In Fig. 7d, the dislocations could be seen folded when interacted with an oxide particle.

The oxides size distributions are shown in Fig. 8. Before irradiation, the diameter of oxides are mainly distributed between 10 and 30 nm, which is in agreement with Ref. [74]. After irradiation, the size distribution slightly moves to a lower range, which suggests that the oxide particles shrink or dissolve during irradiation. The dissolution process is irradiation dose, dose rate and temperature dependent. Generally, higher temperature and higher dose will causeheavier dissolution according to Ref. [75]. A recent study showed increased dissolution of pyrochlore $Y_2Ti_2O_7$ under ion-irradiation at room temperature with increasing damage level (dpa dependence) [76]. In addition, Chen et al. 's work [77] suggests that at lower temperatures, the dissolution will be more significant (temperature dependence), and this behavior may also related to the coherency. The dissolution rate could be retarded by reducing the dose rate, that neutron irradiation might have a lower dissolution rate than ion irradiation. In the current study, the oxides in MA956 exhibit a slight reduction in size after neutron irradiation,

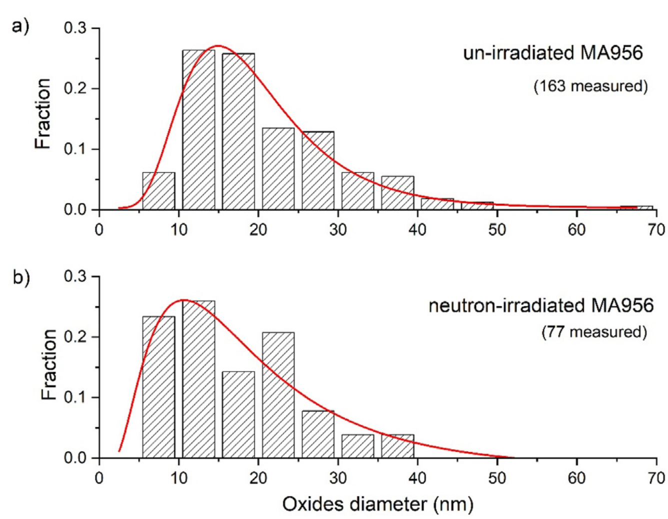

Fig. 8. The oxides diameter distribution of MA956 before and after irradiation.

from an average of 20.1 nm to that of 17.5 nm, but the number density reduced about a half, from ~16.2 × $10^{20}/m^3$ before irradiation to ~8.4 × $10^{20}/m^3$ after irradiation. The reason may be owing to different structure and/or different coherent relations between matrix and oxides leading to different dissolution ability. In general, the oxide particles were considered stable because the order of magnitude didn't change after irradiation. In Fig. 7a, the moiré fringes indicate that the oxides maintained their crystal structure, which means these oxides have good irradiation resistance against amorphization. The number density and size of dislocation lines, loops, voids and oxides before and after irradiation are summarized in Table 2.

3.5. Tensile tests

Tensile tests were performed at CMR in LANL. Two samples were tested at each condition. The results were shown in Fig. 9. The yield stress, uniform tensile strength (UTS), uniform elongation (e_u) and total elongation (e_t) are summarized in Table 3. The unirradiated material has the total elongation (e_{tu}) about 13.70 ± 1.56%. After irradiation, the total elongation (e_{ti}) reduced to 0.90 ± 0.21%. The reduction of elongation (e_{ti}-e_{tu}) corresponds to the yield strength increasing, from 690 MPa before to 1072.5 ± 10.6 MPa after irradiation. The reduction rate is 3.3%/100 MPa. In unirradiated materials, continuous strain hardening occurred after yielding. The post-necking ductility is about 4.7%. For the irradiated specimens, the engineering stress drop down immediately after reaching the yield point. This behavior is similar to several F/M steels but different to HT9, MA957 [78] and 14YWT [37]. Note that MA957 and 14YWT are both Al-free ODS steels with a high density of ultra-fine oxides (~2 nm) in MA957 [79] and 14YWT [67] that reduced the formation of irradiation induced defects, contrasting with the MA956 with coarser oxide particles presented here.

4. Discussion

4.1. Hardening model

Based on the statistical results in Table 2, the irradiation hardening caused by defects could be calculated by dispersed barrier hardening (DBH) using either linear method or root-sum-square (RSS) method.

$$\Delta\sigma_y^{linear} = \sum \Delta\sigma_{line,loop,void,oxide} \quad (8)$$

$$\Delta\sigma_y^{root-sum-square} = \sqrt{\sigma_{line}^2 + \sigma_{loop}^2 + \sigma_{void}^2 + \sigma_{oxide}^2} - \sqrt{\sigma_{unirr\ line,oxide}^2} \quad (9)$$

$$\sigma_{line} = M\alpha\mu b\sqrt{\rho} \quad (10)$$

$$\sigma_{loop,void,oxide} = M\alpha\mu b\sqrt{Nd} \quad (11)$$

Table 2
Summary of defects in MA956 before and after neutron irradiation.

MA956		Average Size(nm)	Density
Irradiated	Dislocation lines	–	10.58 ± 0.94 × 10^{14}/m^2
	Dislocation loops	17.6 ± 10.2	7.17±10^{21}/m^3
	½<111>	16.6 ± 8.4	3.73 × 10^{21}/m^3
	<100>	18.6 ± 19.1	3.44 × 10^{21}/m^3
	Oxides	17.5 ± 8.0	8.37 ± 3.73 × 10^{20}/m^3
	Voids	8.7 ± 2.9	1.80 × 10^{21}/m^3
Unirradiated	Dislocation lines	–	2.72 ± 0.59 × 10^{14}/m^2
	Oxides	20.1 ± 9.6	16.15 ± 0.25 × 10^{20}/m^3

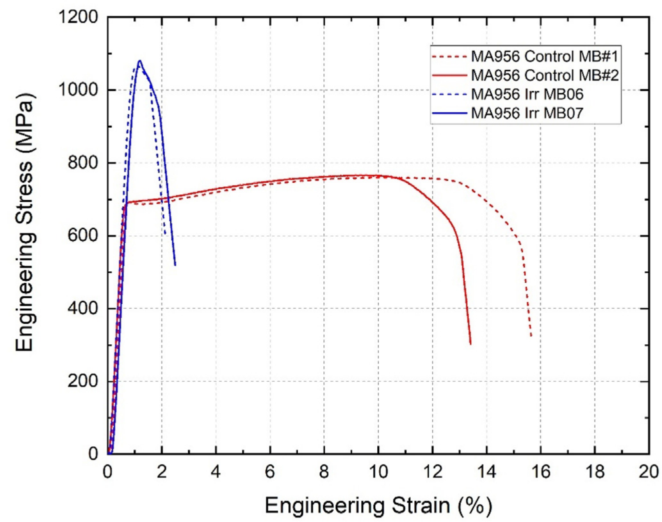

Fig. 9. Tensile test results of control (as-received) and irradiated MA956.

$$\Delta\sigma_{loop}^{linear} = \sigma_{111} + \sigma_{100} \quad (12)$$

$$\Delta\sigma_{loop}^{root-sum-square} = \sqrt{\sigma_{111}^2 + \sigma_{100}^2} \quad (13)$$

Where σ_y is the yield strength, $\Delta\sigma_{line,\ loop,\ void,\ oxide}$ represents the change of yield strength caused by dislocation lines, loops, voids and oxides, respectively. M is the Taylor factor which equals 3.06 for FCC and BCC materials. The hardening factor, α, uses different values for different microstructures. The shear modulus μ is 82 GPa,for FeCrAl ODS steels. The Burgers vector b is 0.249 nm for ½<111> moving dislocation lines. The dislocation line density ρ, number density N and diameter d of loops, voids and oxides are listed in Table 2.

As there are two types of dislocation loops, ½<111> and <100>, in the irradiated MA956, it is important to know the fraction of each type of loop to apply equations 8–13. From Fig. 3, we can briefly identify the Burgers vectors of dislocation loops. However, as the sample is tilted to achieve a two-beam condition and some of the loops may change their directions due to the surface effect, the loops are not always along the calculated orientation. Therefore, we drew the distribution of the long axis direction of the loops to help analyze Burgers vectors. Note that according to the invisible criterion, the actual density should be two times the ½<111> type loops and 3/2 times the <100> type loops in Fig. 3a.

In Fig. 10, the arrows indicate the calculated angle of the dislocation loops with different Burgers vector. There is a small shift of the peak away from the calculated results. This shift is because of specimen tilting, as the calculation supposed the specimen is right on the [001] zone axis. Noticing that the peak of <010> type loops is about four times the <100> type loops, but physically they should have equal probability. There are also some dislocation loops lie along 120° which violated the invisible criterion. Here we take 10°~60° as the ½<111> type loops and 0°~10°, 60°~110°, 150°~180° as the <100> type loops. The result shows fraction of ½<111> is 0.45 and fraction of <100> is 0.55, which means the total fraction of ½<111> is 0.52 and <100> 0.48 if taking account for the invisible dislocation loops.

In equation (11), the hardening factor α for different type loops are considered differently. <100> type of dislocation loops has less mobility than ½<111> loops, thus the former should have a higher

Table 3
Summary of tensile test results of MA956.

Type	ID	Yield (MPa)		UTS (MPa)		Uniform elongation (%)		Total elongation (%)		Test temp	Dose (dpa)	Irradiation Temp
Control	MB#1c	690	Avg. 690.0 ± 0.0	760	Avg. 763.0 ± 4.2	9.45	Avg. 9.08 ± 0.52	14.8	Avg. 13.70 ± 1.56	RT	–	–
	MB#2c	690		766		8.72		12.6			–	–
Irradiated	MB06	1065	Avg. 1072.5 ± 10.6	1067	Avg. 1074.0 ± 9.9	0.23	Avg. 0.22 ± 0.01	0.75	Avg. 0.90 ± 0.21	RT	4.36	328 °C
	MB07	1080		1081		0.21		1.05				

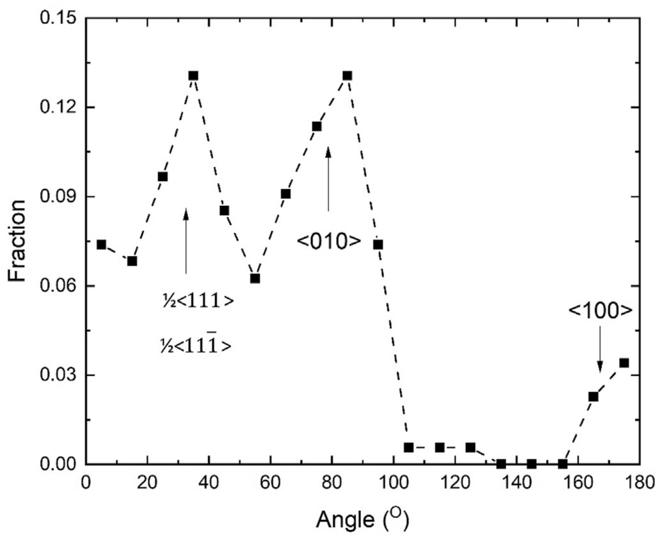

Fig. 10. The distribution of long axis orientation of projected dislocation loops in Fig. 3. X axis stands for the angle between long axis of loop projection and horizontal line (x positive) and Y is the loop fraction.

hardening factor than the latter. In Refs. [54], the α value for ½<111> is chosen as 0.17 and <100> 0.33 in the root-sum-square model while ½<111> 0.05 and <100> 0.31 in linear model. A different set of α was used in nano-indentation measured hardening [80], where the contribution of cavities was ignored which means the α for cavities is 0, and the α is 0.212 for all the other microstructures. In the following calculation, we adopted hardening factor 0.17 and 0.33 for ½<111> and <100> loops, and 0.2 for all the others.

The calculated hardening was listed in Table 4. The <100> loops and dislocation lines contribute the most to the total increase in yielding stress, with 165 MPa and 200 MPa respectively. The oxides due to shrink in size and decrease in density, have negative contribute to hardening. The calculated results are compared to tensile experiments. The total calculated hardening is 475 MPa by linear method and 234 MPa by RSS method. The underestimation by RSS method is owing to ignorance of α′ precipitates. Although α′ was considered to be weak barriers, the high density of α′ precipitate could yield dominant contribution to the hardening [54]. The compensation of hardening from α' precipitate is estimated to be 395 MPa. However, it might be overestimated again because of the hardening factor selection for other defects is not fully convincible by current limited data.

The linear method overestimated hardening, as shown in Table 4. This is not a favored method because doubled number density will not yield doubled hardening in equation (11). The linear method only works when a particular type of defects plays dominant role in the hardening. In Table 4, the hardening from <100> loops and dislocation lines are pretty similar, resulting in the overestimation of linear-calculated hardening.

4.2. Space distribution of dislocation lines

If a dislocation loop grows and meets a boundary of a grain surface, the loop circuit will open and become a dislocation line. Dislocation lines could act as a biased sink of point defects generated from irradiation. The dislocation line density is $2.72 \times 10^{14}/m^2$ in unirradiated materials and $10.58 \times 10^{14}/m^2$ after irradiation. The dislocation lines with high density could form into tangles during irradiation, however, it could be just an overlap of images such that the dislocation lines are separated in space indeed. To identify whether the dislocations are tangled, stereo scan of the specimen in TEM was performed. Fig. 11a shows the initial position and the scale bar of this field in STEM mode. The diffraction condition is given in Fig. 11b, where the systematic row was quickly scanned by a side-mount wide angle CCD camera. To keep the images under the same diffraction condition, the tilting was designed to be normal to g=(110) as much as possible. Nevertheless, while the tilting angle went larger, the Kikuchi line deviated far away from its original position, that the contrast of the dislocations became variable in the tilting direction.

Figs. 11c and d are zoomed ROI of the dashed box in Fig. 11a. The red and blue lines present for the overlapped dislocation respectively. After 5° tilted from Fig.11c to d, the red line moved to the right and the point of interaction migrated to the upper right consequently. This phenomenon indicates these two lines are not intersected in space. Supplement S1 shows the animation of dislocations while tilting. Each frame in this GIF file was +1° tilted then reverse displayed. In animation S1, the dislocation lines were found with changing the crossover position during tilting, which means these dislocations are seldom tangled with each other in 3D space.

Table 4
Compare of experiment and calculated hardening.

	factor α	Cal. Δσ (MPa)	Cal. Linear (MPa)	Cal. RSS (MPa)	Exp. $\Delta\sigma_y$ (MPa)
½<111> loops	0.17	83.6	475	234	382
<100> loops	0.33	165			
voids	0.2	49.4			
Dis. lines	0.2	200			
Oxides	0.2	−23.4			
Unknown (fine precipitates)		Estimated 395 MPa			

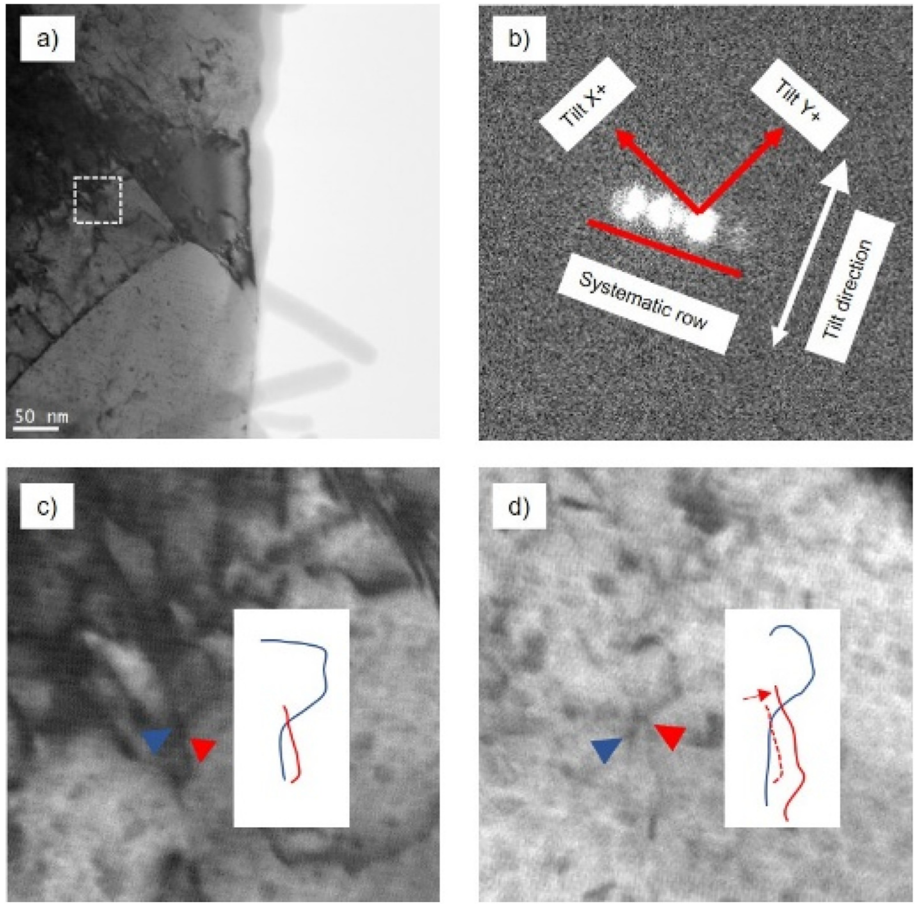

Fig. 11. Changes in position of dislocation overlap respect to different tilt angles: a) initial position and b) the systematic row in STEM mode, c) the zoomed image of the dashed box and d) after 5° tilted. (Full animation is attached in the supplements).

5. Conclusions

MA956 is an iron-chromium-aluminum (FeCrAl) based oxide dispersion strengthened (ODS) alloy produced by mechanical alloying. The alloy was irradiated in Advanced Test Reactor (ATR) at 328 °C up to 4.36 dpa with both thermal and fast neutrons. The microstructures of MA956 before and after irradiation were investigated via various TEM techniques.

Dislocation loops were formed during neutron irradiation. The density of dislocation loops was $7.17 \times 10^{21}/m^3$. The mean size of dislocation loops was 17.6 ± 10.2 nm, while the largest ones could reach to over 60 nm. The distribution obeys lognormal fitting. Both 1/2<111> and <100> loops existed in irradiated materials according to the projection in STEM-BF images. islocation lines are demonstrated not forming tangles in irradiated specimens by stereo scanning. Voids were formed during irradiation. Argon bubbles were observed in unirradiated materials attached to the surface of oxide particles. The swelling rate was estimated to be 0.08% without subtracting the Ar bubbles.

The oxides showed small shrinkage in size with decrease in number density by 50% after irradiation. Dissolution may have occurred during irradiation. No amorphization was observed. The oxides are Y—Al—O types, with an average diameter of 20.1 ± 9.6 nm before and 17.5 ± 8.0 nm after irradiation.

Tensile test showed hardening and ductility reduction after irradiation. The reduction rate is 3.3%/100 MPa. Hardening was estimated by DBH model using both linear and root-sum-square method. Result showed <100> loops and dislocation lines contributed most to the irradiation hardening. α' precipitates were considered as contributor to the hardening, even not observed in EFTEM method.

Based on the results we can conclude the oxides in MA956 could maintain crystal structure but partially dissolved in the experiment temperature range. Some suggestions are made here. First, as the swelling and irradiation embrittlement are issues for the irradiation, additional bearing element like Zr may mitigate this problem by refining size of oxides. Second, the high Cr concentration in MA956 have the alpha prime precipitate problem. Reduced Cr is recommended for cladding ferritic ODS steels design.

Declaration of competing interest

There are no conflicts of interest to declare.

CRediT authorship contribution statement

Zhexian Zhang: Methodology, Software, Validation, Formal analysis, Investigation, Data curation, Writing - original draft, Writing - review & editing. **Tarik A. Saleh:** Conceptualization, Methodology, Validation, Investigation, Resources, Data curation, Writing - review & editing. **Stuart A. Maloy:** Conceptualization, Methodology, Validation, Resources, Writing - review & editing, Supervision, Project administration, Funding acquisition. **Osman Anderoglu:** Conceptualization, Methodology, Validation, Investigation, Writing - original draft, Writing - review & editing.

Acknowledgement

This research is supported by NEUP (grant No. DE-NE0008656) and NRC faculty development grants (No. NRC-HQ-60-17-G-0007). The authors also acknowledge partial funding from the Advanced Fuels Campaign of the Department of Energy's Nuclear Technology R&D Program. The MA-956 was irradiated in the UCSB ATR-1 irradiations that were carried out as part of the National Scientific Users Facility program.

Appendix A. Supplementary data

Supplementary data to this article can be found online at https://doi.org/10.1016/j.jnucmat.2020.152094.

References

[1] W. Beck, P. Blanpain, T. Fuketa, A. Gorzel, Z. Hozer, K. Kamimura, Y.-H. Koo, D. Maertens, O. Nechaeva, M. Petit, Nuclear Fuel Safety Criteria Technical Review, 2012.

[2] International Atomic Energy Agency, Structural Materials for Liquid Metal Cooled Fast Reactor Fuel Assemblies-Operational Behaviour, IAEA, Vienna, 2012.

[3] Oecd-Nea, State-of-the-Art Report on Light Water Reactor Accident-Tolerant Fuels, 2018. No.7317.

[4] S.J. Zinkle, K.A. Terrani, J.C. Gehin, L.J. Ott, L.L. Snead, Accident tolerant fuels for LWRs: a perspective, J. Nucl. Mater. 448 (2014) 374–379, https://doi.org/10.1016/j.jnucmat.2013.12.005.

[5] B.A. Pint, K.A. Terrani, Y. Yamamoto, L.L. Snead, Material selection for accident tolerant fuel cladding, Metall. Mater. Trans. E. 2 (2015) 190–196, https://doi.org/10.1007/s40553-015-0056-7.

[6] H.G. Kim, J.H. Yang, W.J. Kim, Y.H. Koo, Development status of accident-tolerant fuel for light water reactors in korea, Nucl. Eng. Technol. 48 (2016) 1–15, https://doi.org/10.1016/j.net.2015.11.011.

[7] G.S. Was, D. Petti, S. Ukai, S. Zinkle, Materials for future nuclear energy systems, J. Nucl. Mater. 527 (2019) 151837, https://doi.org/10.1016/j.jnucmat.2019.151837.

[8] S. Ukai, S. Ohtsuka, T. Kaito, Y. de Carlan, J. Ribis, J. Malaplate, Oxide dispersion-strengthened/ferrite-martensite steels as core materials for generation IV nuclear reactors, in: Struct. Mater. Gener. IV Nucl. React., Elsevier, 2017, pp. 357–414.

[9] Oecd-Nea, K. Pasamehmetoglu, S. Massara, D. Costa, S. Bragg-Sitton, M. Moatti, M. Kurata, D. Iracane, T. Ivanova, J. Bischoff, C. Delafoy, State-of-the-Art Report on Light Water Reactor Accident-Tolerant Fuels, 2018. No.7317.

[10] K.A. Terrani, S.J. Zinkle, L.L. Snead, Advanced oxidation-resistant iron-based alloys for LWR fuel cladding, J. Nucl. Mater. 448 (2014) 420–435, https://doi.org/10.1016/j.jnucmat.2013.06.041.

[11] G.R. Odette, On the status and prospects for nanostructured ferritic alloys for nuclear fission and fusion application with emphasis on the underlying science, Scripta Mater. 143 (2018) 142–148, https://doi.org/10.1016/j.scriptamat.2017.06.021.

[12] G.R. Odette, D.T. Hoelzer, Irradiation-tolerant nanostructured ferritic alloys: transforming helium from a liability to an asset, JOM (J. Occup. Med.) 62 (2010) 84–92.

[13] G.R.R. Odette, M.J.J. Alinger, B.D.D. Wirth, Recent developments in irradiation-resistant steels, Annu. Rev. Mater. Res. 38 (2008) 471–503, https://doi.org/10.1146/annurev.matsci.38.060407.130315.

[14] S.J. Zinkle, J.T. Busby, Structural materials for fission & fusion energy, Mater. Today 12 (2009) 12–19, https://doi.org/10.1016/S1369-7021(09)70294-9.

[15] A. Kimura, R. Kasada, N. Iwata, H. Kishimoto, C.H. Zhang, J. Isselin, P. Dou, J.H. Lee, N. Muthukumar, T. Okuda, M. Inoue, S. Ukai, S. Ohnuki, T. Fujisawa, T.F. Abe, Development of Al added high-Cr ODS steels for fuel cladding of next generation nuclear systems, J. Nucl. Mater. 417 (2011) 176–179, https://doi.org/10.1016/j.jnucmat.2010.12.300.

[16] J. Ejenstam, M. Thuvander, P. Olsson, F. Rave, P. Szakalos, Microstructural stability of Fe-Cr-Al alloys at 450-550 °C, J. Nucl. Mater. 457 (2015) 291–297, https://doi.org/10.1016/j.jnucmat.2014.11.101.

[17] P. Song, Z. Zhang, K. Yabuuchi, A. Kimura, Helium bubble formation behavior in ODS ferritic steels with and without simultaneous addition of Al and Zr, Fusion Eng. Des. 125 (2017), https://doi.org/10.1016/j.fusengdes.2017.03.139.

[18] P. Song, A. Kimura, K. Yabuuchi, P. Dou, H. Watanabe, J. Gao, Y.J. Huang, Assessment of phase stability of oxide particles in different types of 15Cr-ODS ferritic steels under 6.4 MeV Fe ion irradiation at 200 °C, J. Nucl. Mater. 529 (2020) 151953, https://doi.org/10.1016/j.jnucmat.2019.151953.

[19] R.B. Rebak, Accident Tolerant Materials for Light Water Reactor Fuels, Elsevier, 2020.

[20] M. Snead, L.L. Snead, K.A. Terrani, K.G. Field, A. Worrall, K.R. Robb, Y. Yamamoto, J. Powers, S. Dryepondt, B.A. Pint, X. Hu, Technology Implementation Plan ATF FeCrAl Cladding for LWR Application, 2015.

[21] Special Metals, INCOLOY alloy MA956. http://216.71.103.52/documents/Incoloy alloy MA956.pdf, 2004.

[22] T.S. Chou, H.K.D.H. Bhadeshia, Recrystallization temperatures in mechanically alloyed oxide-dispersion-strengthened MA956 and MA957 steels, Mater. Sci. Eng. 189 (1994) 229–233, https://doi.org/10.1016/0921-5093(94)90419-7.

[23] J. Chao, M.M. Aranda, R. Rementeria, M. Serrano, C. Capdevila, On the anisotropy of the ductile to brittle transition behavior in a wrought and in two oxide dispersion strengthened FeCrAl steels, Metall. Mater. Trans. (2018), https://doi.org/10.1007/s11661-018-5033-1.

[24] G.D. Smith, J.J. Fischer, High temperature corrosion resistance of mechanically alloyed products in gas turbine environments, in: ASME 1990 Int. Gas Turbine Aeroengine Congr. Expo., American Society of Mechanical Engineers, 1990. V005T12A006-V005T12A006.

[25] S. Floreen, R.H. Kane, T.J. Kelly, M.L. Robinson, An evaluation of incoloy alloy MA 956 for high temperature gas cooled reactor systems, J. Mater. Energy Syst. 2 (1980) 15–24.

[26] W.J. Quadakkers, Growth mechanisms of oxide scales on ODS alloys in the temperature range 1000–1100 C, Mater, Corrosion 41 (1990) 659–668, https://doi.org/10.1002/maco.19900411204.

[27] T. Hosoda, Microstructure and Texture Evolution in Cold-Rolled and Annealed Alloy MA-956, Colorado School of Mines, 2014.

[28] A. Czyrska-Filemonowicz, B. Dubiel, Mechanically alloyed, ferritic oxide dispersion strengthened alloys: structure and properties, J. Mater. Process. Technol. 64 (1997) 53–64.

[29] J.S. Benjamin, Mechanical alloying, Sci. Am. 234 (1976) 40–49.

[30] J. Chao, R. Rementeria, M. Aranda, C. Capdevila, J.L. Gonzalez-Carrasco, Comparison of ductile-to-brittle transition behavior in two similar ferritic oxide dispersion strengthened alloys, Materials 9 (2016), https://doi.org/10.3390/ma9080637.

[31] T. Chen, H. Kim, J.G. Gigax, D. Chen, C. Wei, F.A. Garner, L. Shao, Nuclear instruments and methods in physics research B radiation response of oxide-dispersion-strengthened alloy MA956 after self-ion irradiation, Nucl. Instrum. Methods Phys. Res. B. 409 (2017) 259–263, https://doi.org/10.1016/j.nimb.2017.05.024.

[32] J.P. Wharry, M.J. Swenson, K.H. Yano, A review of the irradiation evolution of dispersed oxide nanoparticles in the b.c.c. Fe-Cr system: current understanding and future directions, J. Nucl. Mater. 486 (2017) 11–20, https://doi.org/10.1016/j.jnucmat.2017.01.009.

[33] E. Getto, B. Baker, B. Tobie, S. Briggs, K. Hattar, K. Knipling, Effect of friction stir welding and self-ion irradiation on dispersoid evolution in oxide dispersion strengthened steel MA956 up to 25 dpa, J. Nucl. Mater. 515 (2019) 407–419, https://doi.org/10.1016/j.jnucmat.2018.12.040.

[34] L.L. Hsiung, M.J. Fluss, S.J. Tumey, B.W. Choi, Y. Serruys, F. Willaime, A. Kimura, Formation mechanism and the role of nanoparticles in Fe-Cr ODS steels developed for radiation tolerance, Phys. Rev. B Condens. Matter 82 (2010) 1–13, https://doi.org/10.1103/PhysRevB.82.184103.

[35] C.H. Zhang, J. Jang, H.D. Cho, Y.T. Yang, Void swelling in MA956 ODS steel irradiated with 122 MeV Ne-ions at elevated temperatures, J. Nucl. Mater. 386–388 (2009) 457–461, https://doi.org/10.1016/j.jnucmat.2008.12.161.

[36] D.S. Gelles, Microstructural examination of commercial ferritic alloys at 200 dpa, J. Nucl. Mater. 233–237 (1996) 293–298, https://doi.org/10.1016/S0022-3115(96)00222-X.

[37] D.L. Krumwiede, T. Yamamoto, T.A. Saleh, S.A. Maloy, G.R. Odette, P. Hosemann, Direct comparison of nanoindentation and tensile test results on reactor-irradiated materials, J. Nucl. Mater. 504 (2018) 135–143, https://doi.org/10.1016/j.jnucmat.2018.03.021.

[38] Irradiation Test Plan for the ATR National Scientific User Facility - Univeristy of California Santa Barbara, Idaho National Lab Irradiation Test Plan, Project 29607, PLN 2996, (n.d.).

[39] B.D.R. De, J.B.H. Leonard, Advanced Test Reactor, 1964.

[40] FY 2009 Advanced Test Reactor National Scientific User Facility Users' Guide, 2009.

[41] P.J. Phillips, M.C. Brandes, M.J. Mills, M. De Graef, Ultramicroscopy Diffraction contrast STEM of dislocations : imaging and simulations, Ultramicroscopy 111 (2011) 1483–1487, https://doi.org/10.1016/j.ultramic.2011.07.001.

[42] P.J. Phillips, M.J. Mills, M. De Graef, Systematic Row and Zone axis STEM Defect Image Simulations, 2011, p. 6435, https://doi.org/10.1080/14786435.2010.547526.

[43] C.M. Parish, K.G. Field, Application of STEM characterization for investigating radiation effects in BCC Fe-based alloys, 30, 2015, pp. 1275–1289, https://doi.org/10.1557/jmr.2015.32.

[44] R.F. Egerton, S.C. Cheng, Measurement of local thickness by electron energy-loss spectroscopy, Ultramicroscopy 21 (1987) 231–244, https://doi.org/10.1016/0304-3991(87)90148-3.

[45] T.W.W. Butler, On the Determination of Dislocation Densities, NAVAL ACADEMY ANNAPOLIS MD DEPT OF ENGINEERING, 1969.

[46] S. Pal, M.E. Alam, S.A. Maloy, D.T. Hoelzer, G.R. Odette, Texture evolution and microcracking mechanisms in as-extruded and cross-rolled conditions of a 14YWT nanostructured ferritic alloy, Acta Mater. 152 (2018) 338–357, https://doi.org/10.1016/j.actamat.2018.03.045.

[47] M. Klimiankou, R. Lindau, A. Möslang, Energy-filtered TEM imaging and EELS study of ODS particles and Argon-filled cavities in ferritic-martensitic steels, Micron 36 (2005) 1–8, https://doi.org/10.1016/j.micron.2004.08.001.

[48] B. Yao, D.J. Edwards, R.J. Kurtz, TEM characterization of dislocation loops in irradiated bcc Fe-based steels, J. Nucl. Mater. 434 (2013) 402–410, https://doi.org/10.1016/j.jnucmat.2012.12.002.

[49] C.T. Rueden, J. Schindelin, M.C. Hiner, B.E. DeZonia, A.E. Walter, E.T. Arena, K.W. Eliceiri, ImageJ2: ImageJ for the next generation of scientific image data, BMC Bioinf. 18 (2017) 529.
[50] A.E.-96 e1, Standard Practice for Neutron Radiation Damage Simulation by Charged Particle Radiation, 2009.
[51] F.A. Garner, M.B. Toloczko, B.H. Sencer, Comparison of swelling and irradiation creep behavior of fcc-austenitic and bcc-ferritic/martensitic alloys at high neutron exposure, J. Nucl. Mater. 276 (2000) 123−142, https://doi.org/10.1016/S0022-3115(99)00225-1.
[52] E.A. Little, D.A. Stow, Void-swelling in irons and ferritic steels: II. An experimental survey of materials irradiated in a fast reactor, J. Nucl. Mater. 87 (1979) 25−39.
[53] M.B. Toloczko, F.A. Garner, V.N. Voyevodin, V. V Bryk, O. V Borodin, V. V Mel, A.S. Kalchenko, Ion-induced swelling of ODS ferritic alloy MA957 tubing to 500 dpa, J. Nucl. Mater. 453 (2014) 323−333, https://doi.org/10.1016/j.jnucmat.2014.06.011.
[54] K.G. Field, X. Hu, K.C. Littrell, Y. Yamamoto, L.L. Snead, Radiation tolerance of neutron-irradiated model Fe e Cr e Al alloys *, J. Nucl. Mater. 465 (2015) 746−755, https://doi.org/10.1016/j.jnucmat.2015.06.023.
[55] D. Chen, A. Kimura, W. Han, H. Je, Age-hardening susceptibility of high-Cr ODS ferritic steels and SUS430 ferritic steel, Fusion Eng. Des. 98−99 (2015) 1945−1949, https://doi.org/10.1016/j.fusengdes.2015.05.078.
[56] M. Bachhav, G. Robert Odette, E.A. Marquis, α' precipitation in neutron-irradiated Fe-Cr alloys, Scripta Mater. 74 (2014) 48−51, https://doi.org/10.1016/j.scriptamat.2013.10.001.
[57] P.D. Edmondson, S.A. Briggs, Y. Yamamoto, R.H. Howard, K. Sridharan, K.A. Terrani, K.G. Field, Irradiation-enhanced α' precipitation in model FeCrAl alloys, Scripta Mater. 116 (2016) 112−116, https://doi.org/10.1016/j.scriptamat.2016.02.002.
[58] E.R. Reese, N. Almirall, T. Yamamoto, S. Tumey, G. Robert Odette, E.A. Marquis, Dose rate dependence of Cr precipitation in an ion-irradiated Fe[sbnd]18Cr alloy, Scripta Mater. 146 (2018) 213−217, https://doi.org/10.1016/j.scriptamat.2017.11.040.
[59] E.R. Reese, M. Bachhav, P. Wells, T. Yamamoto, G. Robert Odette, E.A. Marquis, On α' precipitate composition in thermally annealed and neutron-irradiated Fe- 9-18Cr alloys, J. Nucl. Mater. 500 (2018) 192−198, https://doi.org/10.1016/j.jnucmat.2017.12.036.
[60] W. Han, K. Yabuuchi, A. Kimura, S. Ukai, N. Oono, T. Kaito, T. Torimaru, S. Hayashi, Effect of Cr/Al contents on the 475^{o}C age-hardening in oxide dispersion strengthened ferritic steels, Nucl. Mater. Energy 9 (2016) 610−615, https://doi.org/10.1016/j.nme.2016.05.015.
[61] V. De Castro, E.A. Marquis, S. Lozano-Perez, R. Pareja, M.L. Jenkins, Stability of nanoscale secondary phases in an oxide dispersion strengthened Fe-12Cr alloy, Acta Mater. 59 (2011) 3927−3936, https://doi.org/10.1016/j.actamat.2011.03.017.
[62] K.G. Field, B.D. Miller, H.J.M. Chichester, K. Sridharan, T.R. Allen, Relationship between lath boundary structure and radiation induced segregation in a neutron irradiated 9 wt.% Cr model ferritic/martensitic steel, J. Nucl. Mater. 445 (2014) 143−148, https://doi.org/10.1016/j.jnucmat.2013.10.056.
[63] J.P. Wharry, G.S. Was, A systematic study of radiation-induced segregation in ferritic-martensitic alloys, J. Nucl. Mater. 442 (2013) 7−16, https://doi.org/10.1016/j.jnucmat.2013.07.071.
[64] Z. Lu, R.G. Faulkner, G. Was, B.D. Wirth, Irradiation-induced grain boundary chromium microchemistry in high alloy ferritic steels, Scripta Mater. 58 (2008) 878−881, https://doi.org/10.1016/j.scriptamat.2008.01.004.
[65] W. Xiong, K.A. Grönhagen, J. Ågren, M. Selleby, J. Odqvist, Q. Chen, Investigation of spinodal decomposition in Fe-Cr alloys: CALPHAD modeling and phase field simulation, Solid State Phenom. 172−174 (2011) 1060−1065, https://doi.org/10.4028/www.scientific.net/SSP.172-174.1060.
[66] K.G. Field, K.C. Littrell, S.A. Briggs, Precipitation of α' in neutron irradiated commercial FeCrAl alloys, Scripta Mater. 142 (2018) 41−45, https://doi.org/10.1016/j.scriptamat.2017.08.022.
[67] E. Aydogan, J.S. Weaver, U. Carvajal-Nunez, M.M. Schneider, J.G. Gigax, D.L. Krumwiede, P. Hosemann, T.A. Saleh, N.A. Mara, D.T. Hoelzer, Response of 14YWT alloys under neutron irradiation: a complementary study on microstructure and mechanical properties, Acta Mater. 167 (2019) 181−196, https://doi.org/10.1016/j.actamat.2019.01.041.
[68] S.A. Briggs, P.D. Edmondson, K.C. Littrell, Y. Yamamoto, R.H. Howard, C.R. Daily, K.A. Terrani, K. Sridharan, K.G. Field, A combined APT and SANS investigation of α' phase precipitation in neutron-irradiated model FeCrAl alloys, Acta Mater. 129 (2017) 217−228, https://doi.org/10.1016/j.actamat.2017.02.077.
[69] H. Réglé, Alliages ferritiques 14/20% de chrome renforcés par dispersion d'oxydes : Effets des procédés de mise en forme sur les textures de déformation, la recristallisation et les propriétés de traction, 1994, pp. 6−10.
[70] C.H. Zhang, A. Kimura, R. Kasada, J. Jang, H. Kishimoto, Y.T. Yang, Characterization of the oxide particles in Al-added high-Cr ODS ferritic steels, J. Nucl. Mater. 417 (2011) 221−224, https://doi.org/10.1016/j.jnucmat.2010.12.063.
[71] H. Cama, T. Hughes, Stability of dispersoids in commercially available mechanically alloyed oxide dispersion strengthened alloys after high temperature exposures, Mater. Adv. Power Eng. 1994 (1994) 1497−1506.
[72] N.H. Oono, S. Ukai, S. Hayashi, S. Ohtsuka, T. Kaito, A. Kimura, T. Torimaru, K. Sakamoto, Growth of oxide particles in FeCrAl- oxide dispersion strengthened steels at high temperature, J. Nucl. Mater. 493 (2017) 180−188, https://doi.org/10.1016/j.jnucmat.2017.06.018.
[73] P. Dou, A. Kimura, R. Kasada, T. Okuda, M. Inoue, S. Ukai, S. Ohnuki, T. Fujisawa, F. Abe, TEM and HRTEM study of oxide particles in an Al-alloyed high-Cr oxide dispersion strengthened steel with Zr addition, J. Nucl. Mater. 444 (2014) 441−453, https://doi.org/10.1016/j.jnucmat.2013.10.028.
[74] M.F. Hupalo, M. Terada, A.M. Kliauga, A.F. Padilha, Microstructural characterization of INCOLOY alloy MA, 956, 2003, pp. 505−508, 508.
[75] T.R. Allen, J. Gan, J.I. Cole, M.K. Miller, J.T. Busby, S. Shutthanandan, S. Thevuthasan, Radiation response of a 9 chromium oxide dispersion strengthened steel to heavy ion irradiation, J. Nucl. Mater. 375 (2008) 26−37, https://doi.org/10.1016/j.jnucmat.2007.11.001.
[76] P. Song, J. Gao, K. Yabuuchi, A. Kimura, Ion-irradiation hardening accompanied by irradiation-induced dissolution of oxides in FeCr (Y , Ti) -ODS ferritic steel, J. Nucl. Mater. 511 (2018) 200−211, https://doi.org/10.1016/j.jnucmat.2018.09.007.
[77] T. Chen, J.G. Gigax, L. Price, D. Chen, S. Ukai, E. Aydogan, S.A. Maloy, F.A. Garner, L. Shao, Acta Materialia Temperature dependent dispersoid stability in ion-irradiated ferritic- martensitic dual-phase oxide-dispersion-strengthened alloy : coherent interfaces vs . incoherent interfaces, Acta Mater. 116 (2016) 29−42, https://doi.org/10.1016/j.actamat.2016.05.042.
[78] S.A. Maloy, T.A. Saleh, O. Anderoglu, T.J. Romero, G.R. Odette, T. Yamamoto, S. Li, J.I. Cole, R. Fielding, Characterization and comparative analysis of the tensile properties of five tempered martensitic steels and an oxide dispersion strengthened ferritic alloy irradiated at ≈295 °c to ≈6.5 dpa, J. Nucl. Mater. 468 (2016) 232−239, https://doi.org/10.1016/j.jnucmat.2015.07.039.
[79] X. Liu, Y. Miao, Y. Wu, S.A. Maloy, J.F. Stubbins, Stability of nanoclusters in an oxide dispersion strengthened alloy under neutron irradiation, Scripta Mater. 138 (2017) 57−61, https://doi.org/10.1016/j.scriptamat.2017.05.023.
[80] P. Song, D. Morrall, Z. Zhang, K. Yabuuchi, A. Kimura, Radiation response of ODS ferritic steels with different oxide particles under ion-irradiation at 550 °C, J. Nucl. Mater. 502 (2018), https://doi.org/10.1016/j.jnucmat.2018.02.007.